Research article

Enhanced photocatalytic performance by hybridization of Bi_2WO_6 nanoparticles with honeycomb-like porous carbon skeleton

Siyuan Wang[a], Hua Yang[a,*], Zao Yi[b], Xiangxian Wang[a]

[a] *State Key Laboratory of Advanced Processing and Recycling of Non-ferrous Metals, Lanzhou University of Technology, Lanzhou, 730050, China*
[b] *Joint Laboratory for Extreme Conditions Matter Properties, Southwest University of Science and Technology, Mianyang, 621010, China*

A B S T R A C T

In this work, we have assembled Bi_2WO_6 nanoparticles on the surface of honeycomb-like porous carbon skeleton (PCS) via a hydrothermal route to achieve a new type of PCS@Bi_2WO_6 hybrid composite photocatalysts. The PCS@Bi_2WO_6 hybrid structures are determined by SEM, TEM and XPS characterizations. UV–vis DRS investigation suggests an enhanced visible-light absorption of the PCS@Bi_2WO_6 composites. Transient photocurrent response, EIS and PL spectroscopy characterizations demonstrate that the composites exhibit an efficient separation of photoproduced electron/hole pairs. The photocatalytic performance of the composites were evaluated by using RhB as the model pollutant and simulated sunlight as the light source. It is revealed that the PCS@Bi_2WO_6 hybrid composites manifest much enhanced photocatalytic performance. The 5 wt%PCS@Bi_2WO_6 composite manifests the highest photocatalytic activity, which is ca. 2.1 times as large as that of bare Bi_2WO_6 nanoparticles. This can be mainly ascribed to two factors: (1) The photogenerated electron/hole pairs in Bi_2WO_6 are efficiently separated due to the electron transfer between Bi_2WO_6 and PCS; and (2) PCS induces enhanced visible-light absorption and the visible-light-excited electrons in PCS could also take part in the photocatalytic reactions.

1. Introduction

To date, environmental pollution and energy shortage have become two of the biggest problems that urgently need to be solved. Particularly, the wastewater discharged from chemical industries results in serious contamination of water bodies, which poses a great threat to human health and survival. The most common pollutants in the industrial wastewater include organic dyes and pigments, and most of them are carcinogenic to humans and hardly self-decomposed (Brown and De Vito, 1993; Khataeea and Kasiri, 2010). In the energy shortage context, sunlight has been considered as an important power source that is available for dealing with water pollution. Photocatalysis technology based on semiconductors is particularly interesting since it can utilize solar energy for the ablation of organic dyes, and moreover, this technology allows the complete decomposition of organic dyes into harmless inorganic substances (Zhao et al., 2018a; Xia et al., 2018a; Yan et al., 2018a; Reddy et al., 2019). The photocatalytic degradation of dyes is highly dependent on electrons (e^-) and holes (h^+) photogenerated from semiconductor photocatalysts, as well as their reduction and oxidation capabilities. Recently much work has been devoted to Ti-contained oxide semiconductors as the photocatalysts (Zhao et al.,

2018b; He et al., 2017; Wang et al., 2019a; Akpan and Hameed, 2009). However, due to their wide bandgap (E_g = 3.0–3.3 eV), this class of photocatalysts can only use ultraviolet (UV) light, which occupies merely a minor fraction of the total solar radiation, to drive their photocatalytic activity. Furthermore, only a small fraction of photoexcited e^- and h^+ carriers in the semiconductors are available to participate in the photocatalytic reactions because of the easy recombination of the charge carriers. To develop an excellent photocatalyst that can make the best use of solar energy and possesses a high photocatalytic efficiency, the following two points have to be considered: (1) increasing the visible-light absorption of the photocatalyst and (2) facilitating the separation of photoproduced e^-/h^+ pairs. Thus, various methods have been widely applied to modify semiconductor photocatalysts (Zheng et al., 2017; Xia et al., 2018b; Shirzad-Siboni et al., 2017; Tiwari et al., 2018; Wang et al., 2019b; Tayyebi et al., 2018; Zhao et al., 2019a).

Low-dimensional nanomaterials (e.g. zero-/one-/two-dimensional carbon materials, metal nanoparticles) generally exhibit many interesting physicochemical characteristics. Due to their excellent properties, low-dimensional nanomaterials can be technologically applied in many fields, such as bioimaging, energy conversion, optoelectronic

---

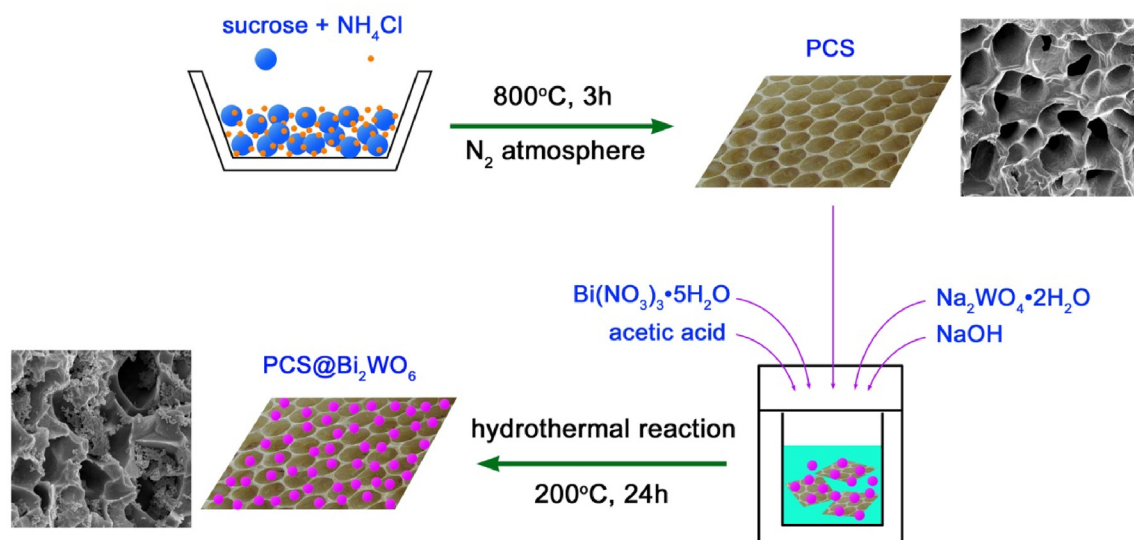* Corresponding author.
  E-mail address: hyang@lut.cn (H. Yang).

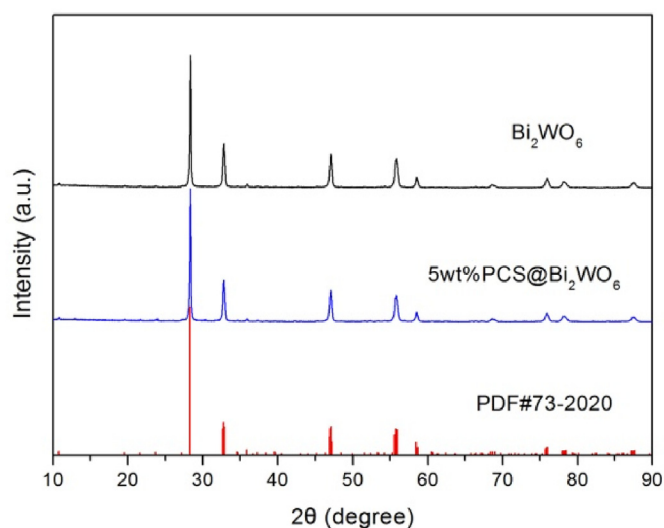Fig. 1. Schematic illustration of the preparation of PCS@Bi$_2$WO$_6$ composites.

Fig. 2. XRD patterns of Bi$_2$WO$_6$ and 5 wt%PCS@Bi$_2$WO$_6$.

devices, wave absorption and sensors (Fernando et al., 2015; Devi1 et al., 2018; Jiang et al., 2018; Cen et al., 2019a,b; Yi et al., 2019a,b; Wang et al., 2019c–e; Tong et al., 2019). More interestingly, these nanomaterials, as excellent modifiers or cocatalysts, have been widely used to modify semiconductor photocatalysts armed at improving their photocatalytic performances (Zhao et al., 2019b; Sharma et al., 2019; Mahdiani et al., 2018; Cruz-Ortiz et al., 2017; Di et al., 2018a; Yan et al., 2019; Tayyebi et al., 2018; Ahmadi et al., 2017). In particular, low-dimensional carbon nanomaterials can act as excellent electron acceptors. This means that when carbon nanomaterials are hybridized with semiconductors, photoproduced electrons in the semiconductors will migrate to the carbon nanomaterials, thus efficiently leading to the e$^-$/h$^+$ pair separation. Furthermore, the carbon nanomaterials have a strong visible-light absorption in the solar spectrum, implying that the hybridization of carbon nanomaterials with semiconductors can significantly enhance the visible light absorption and utilization in the photocatalysis. Up to now, graphene, carbon nanotubes and carbon quantum dots have been frequently used to modify semiconductor photocatalysts (Sharma et al., 2019; Mahdiani et al., 2018; Cruz-Ortiz et al., 2017; Di et al., 2018a). However, there is little work concerned with another type of carbon nanomaterial, honeycomb-like porous

carbon skeleton (PCS), as the photocatalyst modifier. Compared to other carbon nanomaterials, PCS is more efficient at harvesting light by multiple scattering and utilizing photons. It is expected to achieve excellent composite photocatalysts by hybridizing PCS with semiconductors.

Much recent interest has been paid to bismuth tungstate (Bi$_2$WO$_6$) because of its pronounced photocatalytic performance. Bi$_2$WO$_6$ is crystallized in an Aurivillius-type layered structure, and has a special valence band (VB) that is composed of hybrid orbitals of O 2p + Bi 6s (Oshikiri et al., 2002). Owing to its unique crystal structure and band structure, Bi$_2$WO$_6$ manifests a promising photocatalytic degradation of organic pollutants, as well as O$_2$ evolution from water splitting (Chen et al., 2018; Shad et al., 2017; Zhou et al., 2016; Liu et al., 2015; Panmand et al., 2015). Nevertheless, the practical application of Bi$_2$WO$_6$ as a photocatalyst is still limited because it can only be excited by the light with λ < 420 nm and moreover the photon utilization is low due to the easy e$^-$/h$^+$ recombination. To improve its overall photoactivies, Bi$_2$WO$_6$ has been widely modified by various strategies, such as heterostructure construction, impurity element doping, noble metal decoration, surface disorder engineering and carbon material modification (Zheng and Yang, 2018; Ma et al., 2016; Issarapanacheewin et al., 2016; Wang et al., 2019g; Lv et al., 2016; Etogo et al., 2016; Phuruangrat et al., 2015; Yu et al., 2019; Hojamberdiev et al., 2018; Zhang et al., 2017; Kuo et al., 2018). In this work, we designed and prepared a new type of PCS@Bi$_2$WO$_6$ composite photocatalysts by assembling Bi$_2$WO$_6$ nanoparticles on the surface of honeycomb-like PCS. It is demonstrated that the as-prepared PCS@ Bi$_2$WO$_6$ composites exhibit a powerful degradation of rhodamine B (RhB), which is much higher that of bare Bi$_2$WO$_6$ nanoparticles.

2. Experimental

2.1. Preparation of PCS@Bi$_2$WO$_6$ composites

PCS@Bi$_2$WO$_6$ composites composed of Bi$_2$WO$_6$ nanoparticles assembled on the surface of PCS were prepared in two-step methods. In the first step, PCS was prepared via a simple heat-treatment method using sucrose as the precursor. In a typical preparation process, 1 g of sucrose (C$_{12}$H$_{22}$O$_{11}$) and 3 g of ammonium chloride (NH$_4$Cl) were uniformly mixed and ground in an agate mortar. The obtained mixture was loaded in a tubular furnace for the heat-treatment under nitrogen atmosphere (temperature 800 ˚C,time 3 h). During this process, NH$_4$Cl was decomposed into NH$_3$ and HCl, and the formed NH$_3$/HCl gas
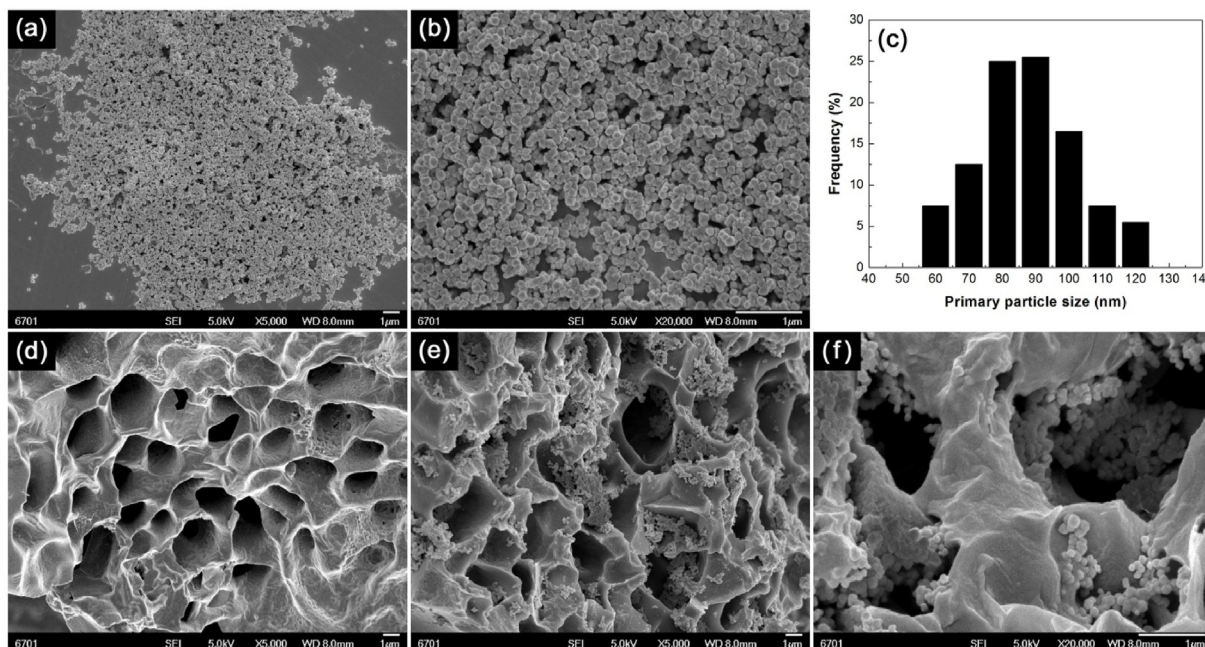
Fig. 3. (a,b) SEM images of bare Bi_2WO_6 particles. (c) Statistical estimation of the primary particle size distribution. (d) SEM image of PCS. (e,f) SEM images of the 5 wt%PCS@Bi_2WO_6 composite.
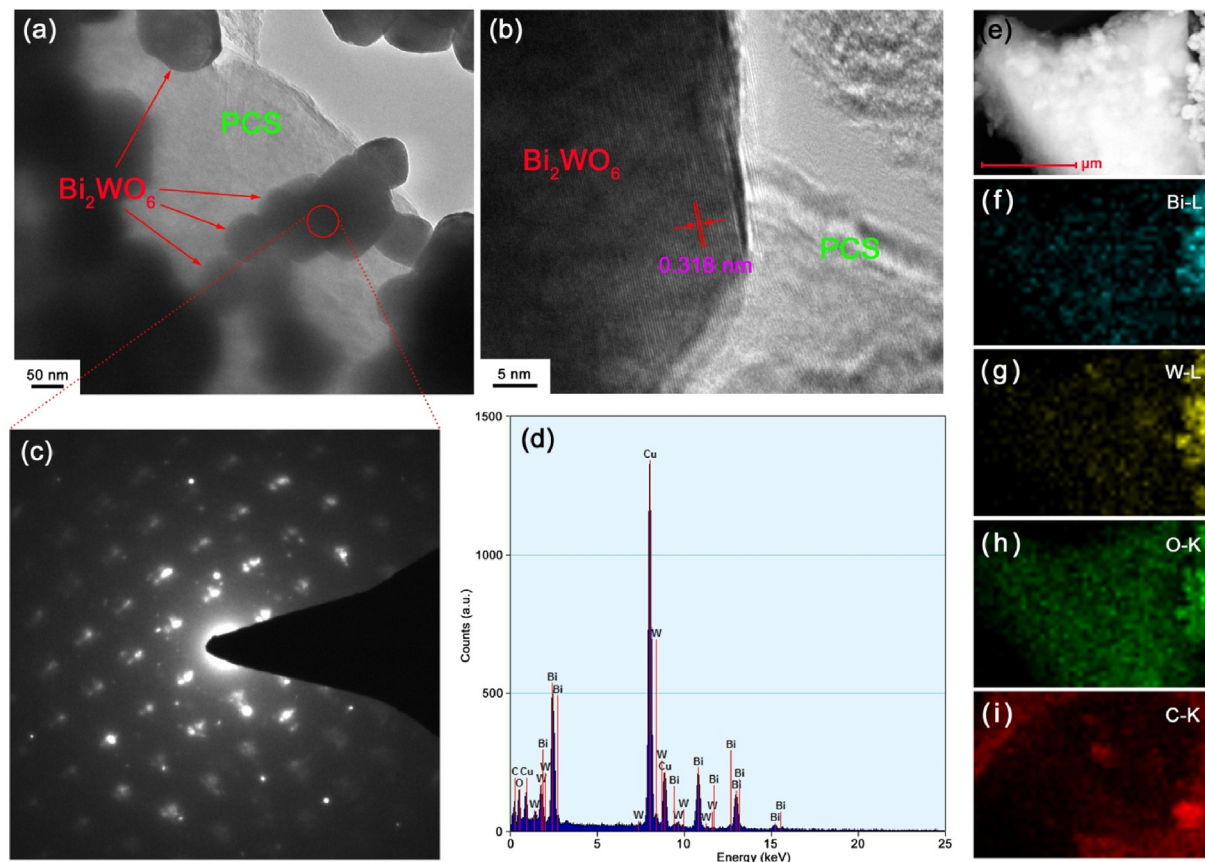

Fig. 4. TEM image (a), high-resolution TEM image (b), SAED pattern (c), EDS spectrum (d), DF-STEM image (e), and energy-dispersive X-ray elemental mapping images (f–i) of the 5 wt%PCS@Bi_2WO_6 composite.

bubbles expanded the melted and carbonized sucrose, and as a result, honeycomb-like porous carbon skeleton was formed. A washing process with deionized water and absolute ethanol was performed to remove the impurities. After drying several hours at 60 °C, the final PCS product was obtained. The second step was to assemble Bi_2WO_6 nanoparticles on the surface of PCS by a hydrothermal method. Typically, acetic acid (3.0025 g, 0.05 mol) and $Bi(NO_3)_3 \cdot 5H_2O$ (0.9702 g, 0.002 mol) were added in deionized water (20 mL) to form solution A. $Na_2WO_4 \cdot 2H_2O$

morphology and microstructure of the samples. The instruments used for the SEM/TEM observations were a JEOL JSM-6701F scanning electron microscope and a JEOL JEM-1200EX transmission electron microscope. Energy-dispersive X-ray spectroscopy (EDS) attached to TEM was use to analyze the chemical composition and elemental distribution of the samples. The N_2 adsorption-desorption technique was used to analyze the Brunauer–Emmett–Teller (BET) area of the samples on a Tristar II 3020 porosimetry analyzer. X-ray photoelectron spectroscopy (XPS) was used to determine the chemical states of elements in the samples on a PHI-5702 multi-functional X-ray photoelectron spectrometer with Mg Kα radiation. The optical absorption and bandgap energy of the samples were characterized by ultraviolet–visible diffuse reflectance spectroscopy (UV–vis DRS) on a TU-1901 double beam UV–vis spectrophotometer. A fluorescence spectrophotometer was used to measure the photoluminescence (PL) spectra of the samples at an excitation wavelength of 315 nm. A CST 350 electrochemical workstation with a three-electrode cell configuration was employed for the photoelectrochemical measurements. The working electrode preparation and measurement procedures were the same as those reported in the literature (Di et al., 2018a, 2018b; Bi et al., 2019). The used electrolyte was 0.1 mol L^{-1} Na$_2$SO$_4$ aqueous solution, and the light source was simulated sunlight emitted from a 200-W xenon lamp. The EIS measurement was carried out by the use of a sinusoidal voltage pulse with amplitude of 5 mV.

2.3. Photocatalytic test

To assess the photocatalytic performance of the samples, RhB aqueous solution (5 mg L^{-1}) was used as the model pollutant and a 200 W xenon lamp was used as the simulated sunlight source. The photocatalyst dosage was 0.1 g in 100 mL RhB solution. Before the photocatalytic experiment, the reaction solution was placed in the dark for 30 min under magnetic stirring to examine the adsorption of RhB on the photocatalyst. At every 30 min of photocatalysis, the RhB concentration was monitored by sampling 2.5 mL of the reaction solution. After removing the photocatalyst by centrifugation, the absorbance of the reaction solution was measured on a UV–vis spectrophotometer at $\lambda = 554$ nm. The degradation efficiency of RhB can be derived according to $D\% = (C_0 - C_t)/C_0 \times 100\%$, where C_0 and C_t are the initial and residual RhB concentration, respectively.

3. Results and discussion

The crystal structures of Bi$_2$WO$_6$ and 5 wt%PCS@Bi$_2$WO$_6$ were determined by XRD patterns, as depicted in Fig. 2. For both the samples, the diffraction peaks including their positions and relative intensities match well with the standard pattern of PDF#73–2020. This implies the synthesis of single orthorhombic Bi$_2$WO$_6$ phase and its structure dose not change when decorated on the surface of PCS. No characteristic peaks of PCS are detected for the 5 wt%PCS@Bi$_2$WO$_6$ composite, which is due to the extremely low content and amorphous feature of PCS.

Fig. 3(a) and (b) display the SEM images of bare Bi$_2$WO$_6$ particles. The statistical estimation of the primary particle size distribution is presented in Fig. 3(c). One can see that the particles have a regularly spherical morphology, and their main size ranges from 60 to 120 nm (average size: 85 nm). The SEM image of PCS depicted in Fig. 3(d) reveals the successive preparation of honeycomb-like porous carbon skeleton. The pore size ranges from 1.5 to 3 μm and the average pore size is ca. 2 μm. Fig. 3(e) and (f) depict the SEM images of the 5 wt% PCS@Bi$_2$WO$_6$ composite, from which Bi$_2$WO$_6$ nanoparticles are clearly seen to be uniformly assembled on the surface of PCS.

The chemical composition and microstructure of the 5 wt%PCS@ Bi$_2$WO$_6$ composite was further investigated by TEM. The TEM image (Fig. 4(a)) demonstrates the good decoration of sphere-like Bi$_2$WO$_6$ nanoparticles (average size: 85 nm) on the surface of PCS. The high-resolution TEM image (Fig. 4(b)) depicts the good crystallization of
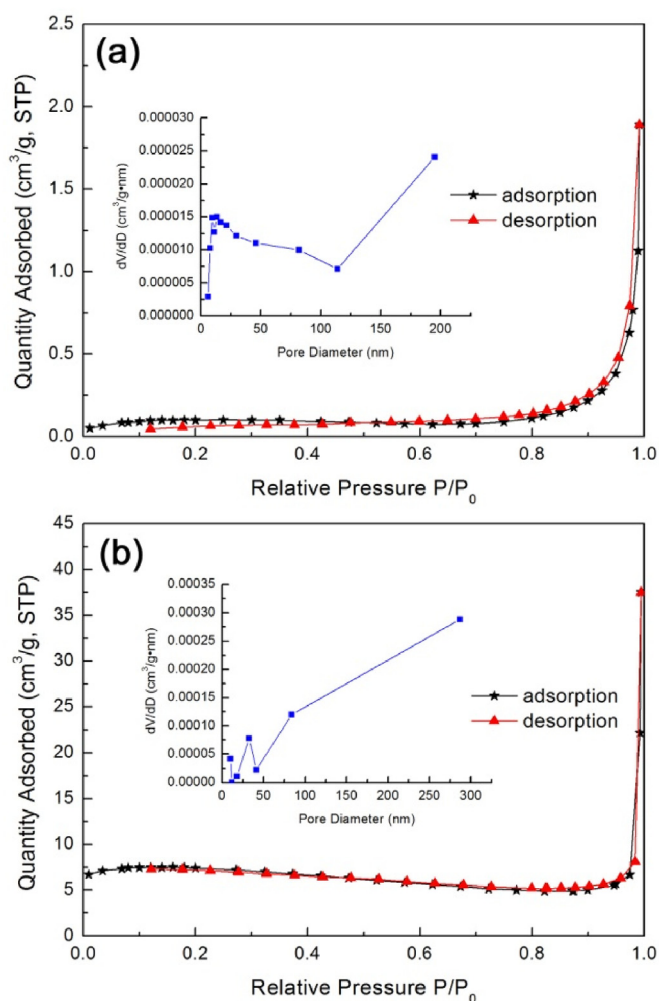

Fig. 5. N_2 adsorption-desorption isotherms of (a) Bi$_2$WO$_6$ and (b) 5 wt%PCS@ Bi$_2$WO$_6$. The insets depict the corresponding pore size distribution curves derived from the adsorption branch of the isotherms using the BJH method.

(0.3298 g, 0.001 mol) was added in deionized water (20 mL) to form solution B. Then solution A was slowly mixed into solution B under mild stirring with a magnetic stirrer. To the above mixture was added 2.2 g (0.055 mol) of NaOH and an amount of deionized water (total volume of the mixture: 70 mL). After 30 min of magnetic stirring, 0.0367 g of PCS was loaded in the mixture solution and magnetically stirred for another 30 min to make PCS uniformly dispersed in the solution. The resultant mixture was put into a Teflon-lined autoclave (100 mL) for the hydrothermal reaction. The reaction temperature was 200 °C and reaction time was 24 h. Deionized water and ethanol was used to wash the product to remove impurities. After 12 h of drying at 60 °C, the final product was obtained as 5 wt%PCS@Bi$_2$WO$_6$ (PCS occupies a mass fraction of 5% in the composite, i.e., m_{PCS}/ ($m_{PCS} + m_{Bi2WO6}$) × 100% = 5%). Fig. 1 shows the flow chart for the preparation of PCS@Bi$_2$WO$_6$ composites. By loading different contents of PCS, we also prepared 2 wt%PCS@Bi$_2$WO$_6$, 8 wt%PCS@Bi$_2$WO$_6$ and 10 wt%PCS@Bi$_2$WO$_6$ composites based on the same experimental procedure.

2.2. Sample characterization

The crystal structure of the samples was identified by means of X-ray powder diffraction (XRD) on a Bruker D8 Advance powder X-ray diffractometer ($\lambda_{CuK\alpha} = 0.15406$ nm). Field-emission scanning/transmission electron microscopy (SEM/TEM) was used to investigate the
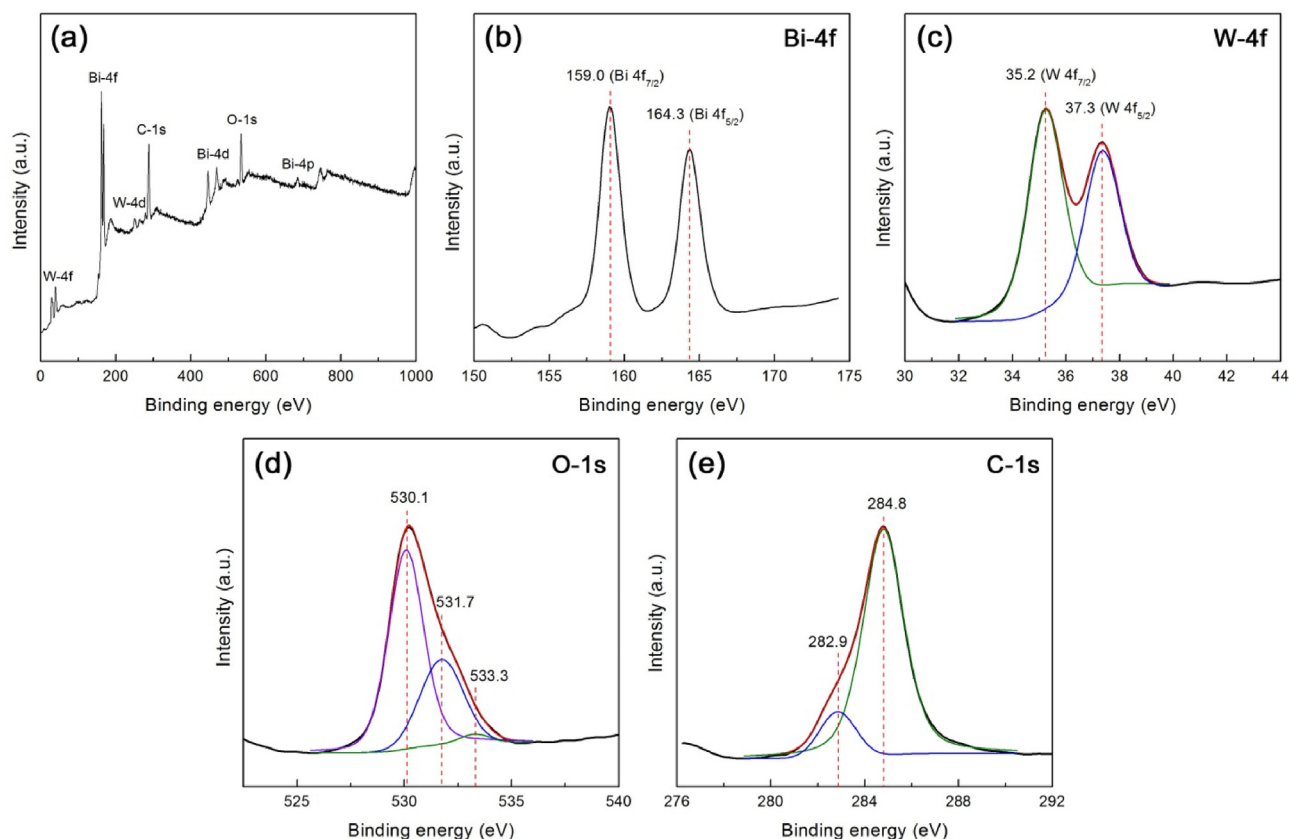
Fig. 6. Survey scan (a), Bi 4f (b), W 4f (c), O 1s (d) and C 1s (e) core-level XPS spectra of 5 wt%PCS@Bi_2WO_6.

Bi_2WO_6 nanoparticles but a amorphous structure for PCS. The observed lattice fringes of 0.318 nm in the d-spacing match perfectly with the (113) crystal plane of Bi_2WO_6. The good crystallization of Bi_2WO_6 can be further confirmed by the selected area electron diffraction (SAED) pattern. As illustrated in Fig. 4(c), obvious diffraction spots being characteristic of orthorhombic Bi_2WO_6 crystals are detected on the SAED pattern. However, these diffraction spots are not regularly arranged in a single lattice period, indicating the possible existence of subgrains in the individual particle. To determine the chemical composition 5 wt%PCS@Bi_2WO_6, its EDS spectrum was measured, as shown in Fig. 4(d). The elements Bi, W, O and C are clearly included in the composite. The observed Cu signal on the EDS spectrum could come from the TEM microgrid holder (Ye et al., 2019). The Bi/W atomic ratio derived from the EDS spectrum agree well with that in the Bi_2WO_6 phase, but the obtained O content is very low. One possible reason is that EDS is not sensitive to light elements like oxygen (Ye et al., 2019). To further elucidate the element distribution of 5 wt%PCS@Bi_2WO_6, energy-dispersive X-ray elemental mappings are obtained in Fig. 4(f)–(i). These mapping images correspond to the dark-field scanning TEM (DF-STEM) image shown in Fig. 4(e). The bright particles on the gray lamella clearly shows the distribution of Bi/W/O elements, and the C-element distribution is observed throughout the lamella. This result further confirms the decoration of Bi_2WO_6 nanoparticles on the surface of PCS.

Fig. 5(a) and (b) show the N_2 adsorption-desorption isotherms of Bi_2WO_6 and 5 wt%PCS@Bi_2WO_6, respectively. Both the isotherms can be characterized as type II based on the IUPAC classification (Sing and Williams, 2004). The desorption and adsorption curves coincides perfectly with each other and no obvious hysteresis loop is observed. This implies minor micro-/meso-/macropores structures exist in the samples. Using the Barrett–Joyner–Halenda (BJH) method, the pore size distribution curves are derived from the adsorption branch of the

isotherms, as shown by the insets in Fig. 5(a) and (b). It is seen that the Y-axis (i.e. dV/dD) values appear very small, further implying the existence of minor micro-/meso-/macropores structures in the samples. The BET surface area of Bi_2WO_6 and 5 wt%PCS@Bi_2WO_6 is obtained as 0.37 and 24.75 $m^2 g^{-1}$, respectively. The much enhanced BET surface area of the composite could be beneficial to the photocatalysis.

XPS analysis was performed on 5 wt%PCS@Bi_2WO_6 to reveal its composition and chemical states of the elements. The XPS survey scan spectrum illustrated in Fig. 6(a) clearly shows the composite includes the Bi, W, O and C elements. Fig. 6(b)–(e) illustrate the high resolution XPS spectra of Bi 4f, W 4f, O 1s and C 1s core levels, respectively. As illustrated in Fig. 6(b), two sharp peaks at 159.0 (Bi $4f_{7/2}$) and 164.3 eV (Bi $4f_{5/2}$) are observed on the Bi 4f XPS spectrum (Wang et al., 2019g; Seddigi et al., 2016; Pooladi et al., 2019). On the W 4f spectrum (Fig. 6(c)), the peaks at 35.2 and 37.3 eV are attributed to the W $4f_{7/2}$ and W $4f_{5/2}$ binding energies (Wang et al., 2019g; Seddigi et al., 2016). No additional Bi 4f and W 4f binding energy peaks are detected on the XPS spectra. This indicates that W species behaves as +6 oxidation state and Bi species behaves as +3 oxidation state. The O 1s XPS spectrum (Fig. 6(d)) is composed of three peaks at 530.1, 531.7 and 533.3 eV, which are contributed by the crystal lattice oxygen of Bi_2WO_6, chemisorbed oxygen species and water species, respectively (Wang et al., 2019g; Seddigi et al., 2016; Pooladi et al., 2019). The C 1s XPS spectrum (Fig. 6(e)) shows two peaks at 284.8 and 282.9 eV. The binding energy peak at 284.8 eV is contributed by the C–C sp2-hybridized carbon of PCS and adventitious carbon that is used for the binding energy scale calibration (Yu and Kwak, 2012; Yan et al., 2018b). The peak at 282.9 eV could be characteristic of the formed carbide (Cheng et al., 1998; Moulder et al., 1992).

It is noted that the photocatalytic performances of semiconductors are highly dependent on their optical absorption properties, which can be determined by UV–vis DRS measurements (Zhang et al., 2019; Wang
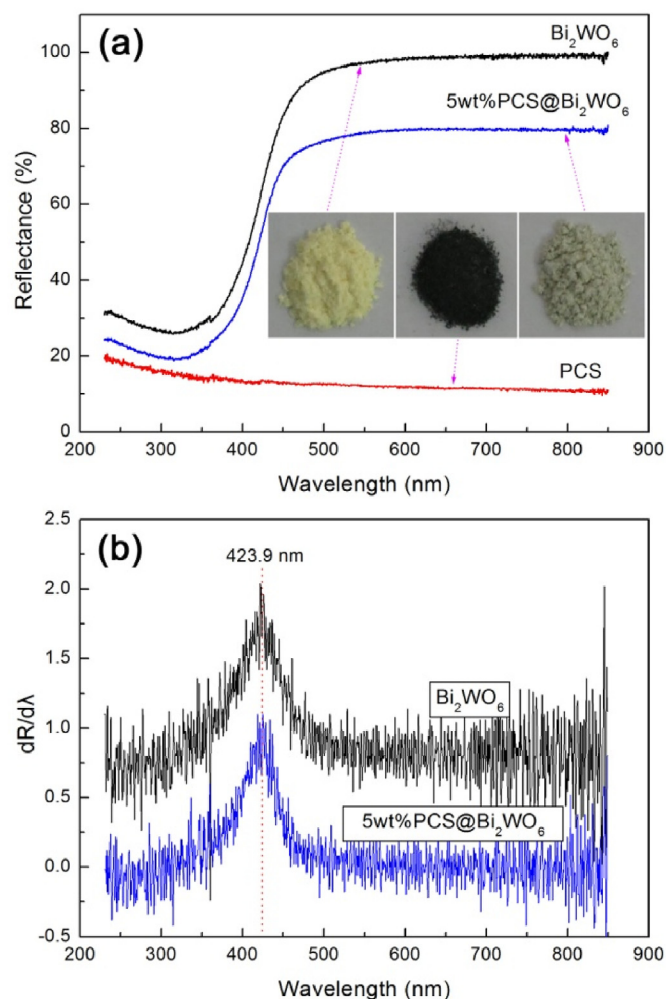
Fig. 7. (a) UV–vis DRS spectra of Bi_2WO_6, 5 wt%PCS@Bi_2WO_6 and PCS, along with the corresponding digital images of the samples (inset). (b) First derivative curves of the UV–vis DRS spectra.
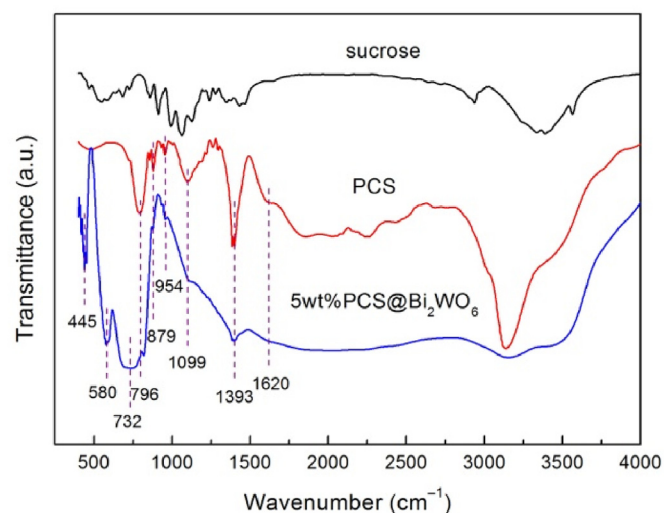

Fig. 8. FTIR spectra of sucrose, PCS and 5 wt%PCS@Bi_2WO_6.

et al., 2019f). Fig. 7(a) depicts the UV–vis DRS spectra of PCS, Bi_2WO_6 and 5 wt%PCS@Bi_2WO_6. It is seen that PCS shows full-spectrum absorption in the measured wavelength range (230–850 nm). Due to the strong light absorption of PCS, the 5 wt%PCS@Bi_2WO_6 composite

therefore manifests enhanced light absorption compared to bare Bi_2WO_6. The digital images of the samples inserted in Fig. 7(a) demonstrate that bare Bi_2WO_6 and PCS manifest a cream-like color and black color, respectively, whereas 5 wt%PCS@Bi_2WO_6 presents a gray color. It is obvious that the 5 wt%PCS@Bi_2WO_6 composite shows a deeper apparent color than bare Bi_2WO_6, confirming that the composite has an enhanced visible-light absorption and thus can utilize sunlight more efficiently during the photocatalysis. To determine the bandgap energy (E_g) of the samples, the first derivative curves of their UV–vis DRS spectra are obtained in Fig. 7(b). The peak on the derivative curves is characteristic of the absorption edge of the samples. A similar absorption edge at 423.9 eV is observed for Bi_2WO_6 and 5 wt%PCS@Bi_2WO_6, from which their E_g is obtained as 2.93 eV according to the relationship $E_g = 1240/\lambda_{abs}$ (λ_{abs} represents the absorption edge wavelength).

Fig. 8 shows the FTIR spectra of sucrose, PCS and 5 wt%PCS@Bi_2WO_6. On the FTIR spectrum of sucrose, numerous absorption peaks or bands being characteristic of sucrose are observed in the region of 500–1500 cm^{-1} (Yang et al., 2018). When sucrose was heat-treated to obtain PCS, the absorption peaks corresponding to sucrose disappear and new absorption peaks are detected on the FTIR spectrum of PCS. The absorption peak at 1620 cm^{-1} is characterized as the C–C stretching vibration (Xie et al., 2017). The observed peaks at 796 and 879 cm^{-1} can be attributed to the C–H deformation vibrations and the peak at 954 cm^{-1} can be assigned to the C–O stretching vibration. This implies the possible formation of C–H and C–O functional groups in PCS. The peaks located at 1393 and 1099 cm^{-1} arise from the O–H in-plane deformation and C–OH stretching vibrations of alcohols left on the sample during the washing process. The presence of NH^{3+} group is confirmed from the broad absorption band centered around 3146 cm^{-1} (N–H stretching vibration) (Mert et al., 2012). For 5 wt%PCS@Bi_2WO_6, additional absorption peaks are detected at 445, 580 and 732 cm^{-1}, which correspond to the Bi–O stretching, W–O stretching and W–O–W bridge stretching modes, respectively (Li et al., 2017; Chong et al., 2017). This suggests that Bi_2WO_6 nanoparticles are successfully assembled on the PCS surface.

Photocurrent response, EIS and PL spectroscopy analyses were performed on Bi_2WO_6 and 5 wt%PCS@Bi_2WO_6 to assess the e^-/h^+ pair separation and transfer behavior. The transient photocurrent response curves are recorded with 10 min irradiation of simulated sunlight followed by 10 min interval, as shown in Fig. 9(a). Both Bi_2WO_6 and 5 wt%PCS@Bi_2WO_6 samples show an obvious photocurrent on the irradiation with simulated sunlight, but a higher photocurrent density is observed for the composite. Fig. 9(b) depicts the EIS spectra (Nyquist plots) of Bi_2WO_6 and 5 wt%PCS@Bi_2WO_6, both of which manifest a shape of a semicircle in the high-frequency region and a straight line in the low-frequency region. The semicircle diameter of the Nyquist plots corresponds to the electrode/electrolyte interface charge-transfer resistance (Wang et al., 2019h; Zhu et al., 2018). The observed smaller semicircle diameter for 5 wt%PCS@Bi_2WO_6 suggests a smaller charge-transfer resistance in the composite. From the photocurrent responses and EIS spectra, it is concluded that a higher separation efficiency of photogenerated e^-/h^+ pairs occurs in the 5 wt%PCS@Bi_2WO_6 composite. This result is further confirmed by the PL spectroscopy analysis. As depicted in Fig. 9(c), a PL emission peak at ca. 580 nm is observed for both Bi_2WO_6 and 5 wt%PCS@Bi_2WO_6, which could arise due to the recombination of photogenerated electron/hole pairs. However, the PL emission peak from 5 wt%PCS@Bi_2WO_6 is obviously lower than that from bare Bi_2WO_6, indicating a decreased electron-hole recombination in the composite.

The Mott-Schottky measurement was performed according to the procedure reported in the literature (Fattah-alhosseini, 2016; Cardon and Gomes, 1978), aimed at determining the conduction band (CB) and VB potentials of Bi_2WO_6 nanoparticles. Fig. 9(d) illustrates the Mott-Schottky plots measured at two voltage frequencies of 3000 and 5000 Hz. The linear portion of the Mott–Schottky plots is extrapolated
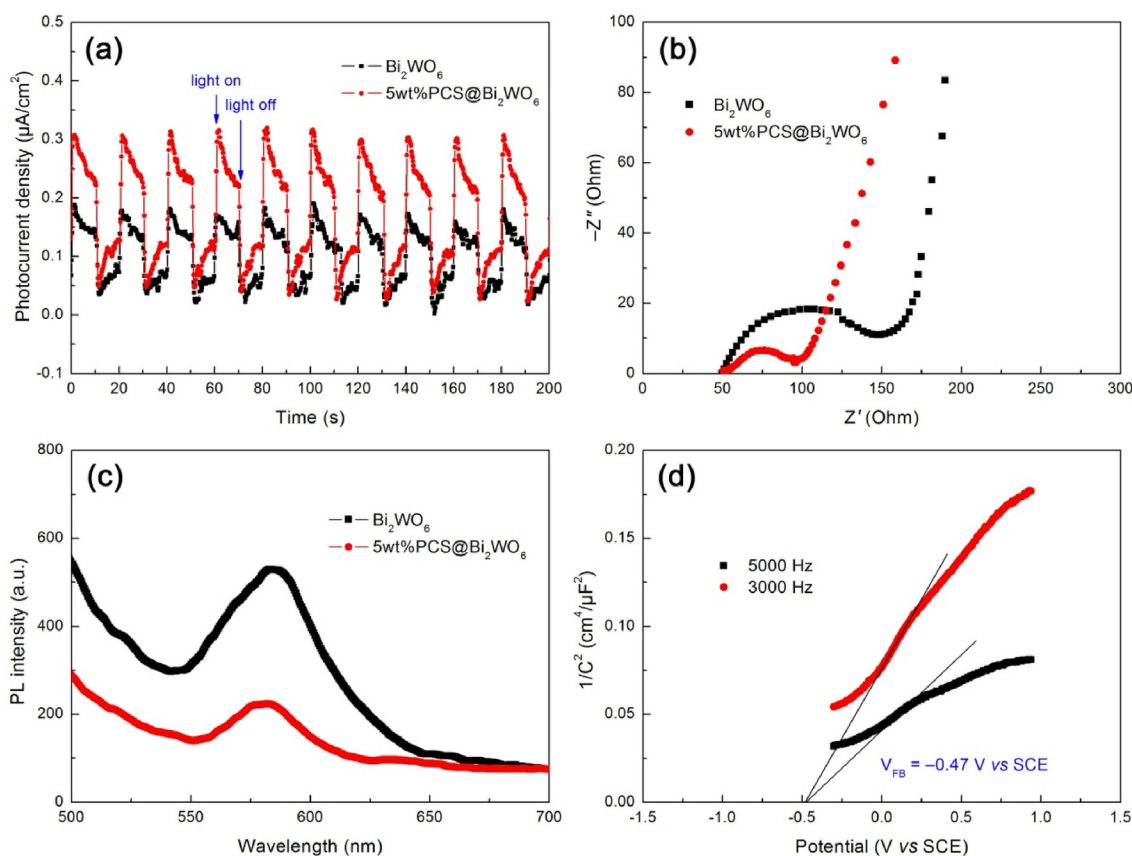
Fig. 9. Photocurrent response curves (a), Nyquist EIS spectra (b), PL spectra (c) and Mott–Schottky plots (d) of Bi_2WO_6 and 5 wt%PCS@Bi_2WO_6.

to the V axis to yield a same flat band potential (V_{FB}) at both frequencies, i.e., −0.47 V vs SCE. The SCE potential can be converted to the potential with reference to normal hydrogen electrode (NHE) according to the relationship: V(NHE) = V(SCE) + 0.059 pH + 0.242 (here pH = 7) (Zhao et al., 2018b). Bi_2WO_6 behaves as an n-type semiconductivity since the Mott–Schottky plots have a positive slope. For an n-type semiconductor, the CB edge potential can be approximately equal to the flat band potential. Thus, the CB and VB potentials of Bi_2WO_6 nanoparticles are estimated as +0.19 and + 3.12 V vs NHE (E_g = 2.93 eV).

To assess the photocatalytic degradation performances of the samples, RhB was chosen as a model pollutant and simulated sunlight was used as the light source. Fig. 10(a) displays the adsorption and photocatalytic degradation of RhB over the samples. The adsorption of RhB on the samples was measured at 30 min of contact time in the dark, and is obtained to be 9.1% for bare Bi_2WO_6. With increasing the PCS content, the dye adsorption on the PCS@Bi_2WO_6 composites gradually increases, and reaches 19.9% for 10 wt%PCS@Bi_2WO_6. It is generally accepted that an appropriate increase in the dye adsorption on the photocatalyst is beneficial to the photocatalytic degradation reactions. Compared to bare Bi_2WO_6, the PCS@Bi_2WO_6 composites exhibit an obviously enhanced photocatalytic activity. The optimal composite sample is observed to be 5 wt%PCS@Bi_2WO_6 with a PCS mass fraction of 5%. This is due to the fact that an appropriate ratio between PCS and Bi_2WO_6 can create the highest level of PCS@Bi_2WO_6 hybrid structures which are beneficial to the enhanced photocatalytic performance. After 180 min illumination, the 5 wt%PCS@Bi_2WO_6 composite photocatalyzes 77.9% degradation of RhB, whereas only 49.5% of the dye is degraded over bare Bi_2WO_6 (see Table 1). The photocatalytic activity between the samples is further compared by the kinetic analysis on the dye degradation. As shown in Fig. 10(b), the plots of $Ln(C_t/C_0)$ vs irradiation time t manifest a good linear relationship, indicating that the

dye degradation process can be perfectly modeled using the pseudo first-order kinetic equation: $Ln(C_t/C_0) = -k_{app}t$ (k_{app} represents the apparent first-order reaction rate constant) (Konstantinou and Albanis, 2004). The value of k_{app} derived from the slope of the regression lines is presented in Table 1, revealing that the optimum composite sample 5 wt%PCS@Bi_2WO_6 (k_{app} = 0.00825 min^{-1}) possesses a photocatalytic activity ca. 2.1 times as large as that of bare Bi_2WO_6 (k_{app} = 0.0039 min^{-1}). The photocatalytic performance of 5 wt%PCS@ Bi_2WO_6 is compared with that of previously reported Bi_2WO_6-based composite photocatalysts toward the RhB degradation, as shown in Table S1, implying that the present 5 wt%PCS@Bi_2WO_6 manifests excellent photocatalytic performance.

To reveal the role of various reactive species in the photocatalysis, the effect of ethanol, benzoquinone (BQ) and ammonium oxalate (AO) on the dye degradation was investigated. Ethanol, BQ and AO were used as the scavengers of hydroxyl (•OH), superoxide (•O_2^-) and photogenerated h$^+$, respectively (Zhao et al., 2019c). 5 mL ethanol, 0.1 mmol BQ and 0.1 mmol AO were separately added into the photocatalytic system (0.1 g of 5 wt%PCS@Bi_2WO_6 + 100 mL of 5 mg L^{-1} RhB solution), and then the photocatalytic degradation experiment was performed in the same procedure without addition of the scavengers. As illustrated in Fig. 10(c), the addition of ethanol has a very small effect on the degradation of RhB, whereas an obvious suppression of the dye degradation is observed with the introduction of AO or BQ. It is concluded from the reactive species trapping experiments that the dye degradation is mainly dependent on the •O_2^- and h$^+$ reactive species, but the role of •O_2^- is relatively larger than that of h$^+$.

The reusability of the 5 wt%PCS@Bi_2WO_6 composite was examined by recycling photocatalytic degradation of RhB. After each photocatalysis cycle, the photocatalyst was collected and recovered by washing with deionized water and drying at 60 °C for 5 h. The recovered photocatalyst was used for the next cycle of the photocatalytic
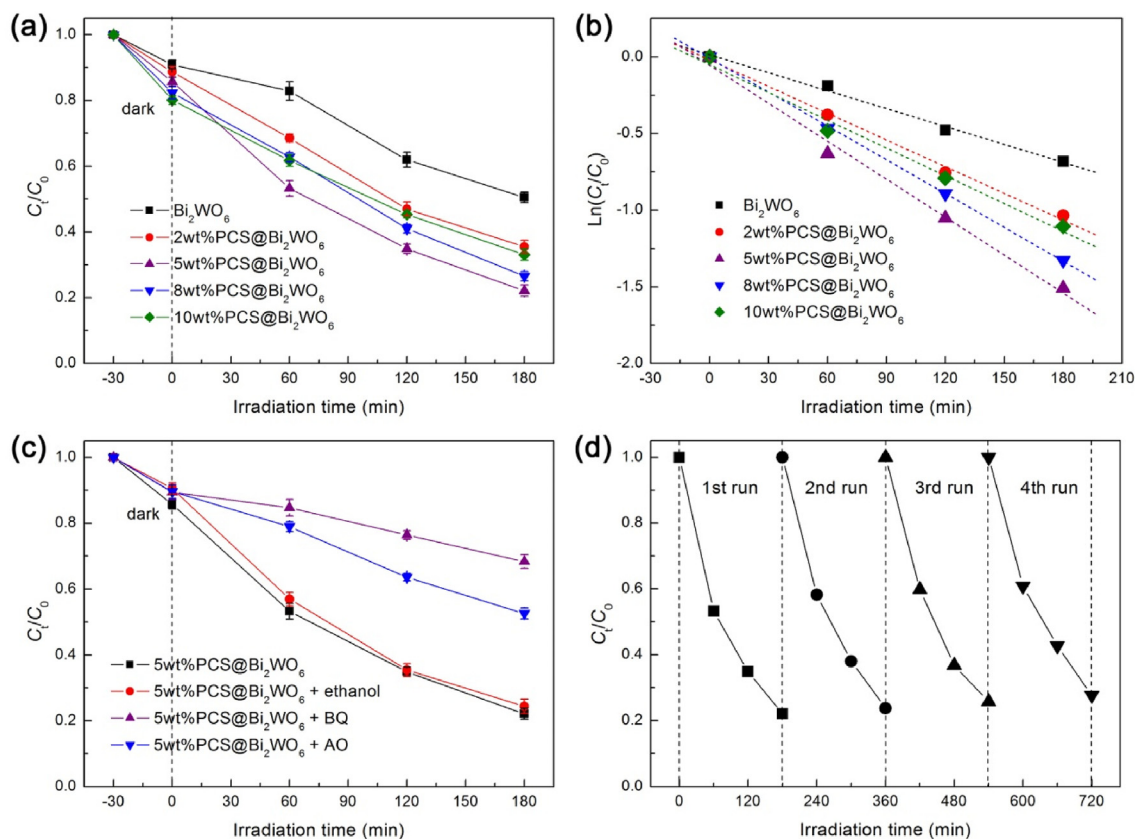
Fig. 10. (a) Time-dependent photocatalytic degradation of RhB over Bi_2WO_6 and the $PCS@Bi_2WO_6$ composites with different PCS contents under simulated sunlight irradiation. (b) Plots of $Ln(C_t/C_0)$ vs irradiation time t for the RhB degradation photocatalyzed by the samples. (c) Effect of ethanol, BQ and AO on the degradation of RhB over 5 wt%$PCS@Bi_2WO_6$. (d) Recycling ability of 5 wt%$PCS@Bi_2WO_6$ toward the photocatalytic degradation RhB.

Table 1
Degradation percentage of RhB (reaction for 180 min) and apparent first-order reaction rate constant k_{app} for Bi_2WO_6 and the $PCS@Bi_2WO_6$ composites.

Samples	Degradation (%)	k_{app} (min^{-1})
Bi_2WO_6	49.5	0.0039
2 wt%$PCS@Bi_2WO_6$	64.5	0.00581
5 wt%$PCS@Bi_2WO_6$	77.9	0.00825
8 wt%$PCS@Bi_2WO_6$	73.5	0.00735
10 wt%$PCS@Bi_2WO_6$	66.9	0.00604

experiment under the same conditions. As seen from Fig. 10(d), the 5 wt%$PCS@Bi_2WO_6$ composite shows a good stability for the photocatalytic degradation of RhB. After reaction for 180 min, the degradation percentage of RhB is about 77.9% and 72.3% at the 1st and 4th cycles of the photocatalysis, respectively, indicating a loss of only 4.7% of the dye degradation.

Fig. 11 schematically shows the photocatalytic mechanism of $PCS@Bi_2WO_6$ toward the dye degradation. Under simulated sunlight irradiation, electrons in the VB of Bi_2WO_6 are excited to its CB, simultaneously creating holes in its VB. PCS can also undergo the electronic excitation, i.e., electrons in a low-energy state (e.g. the highest occupied molecular orbital, HOMO) are excited to a high-energy state (e.g. the lowest unoccupied molecular orbital, LUMO) (Li et al., 2012). The photoexcited PCS can be acted as a good electron donor and acceptor. Consequently, the CB electrons of Bi_2WO_6 will migrate to the HOMO of PCS, and conversely the photoexcited electrons in the LUMO of PCS will transfer to the CB of Bi_2WO_6. This electron excitation and transfer process is very similar to the case occurring in the carbon quantum dots modified semiconductor photocatalysts (Li et al., 2012). Due to the interesting electron transfer process, the recombination of the

photogenerated electrons and holes in Bi_2WO_6 can be efficiently suppressed, resulting in more photogenerated carriers participating in the photocatalytic reactions. As a result, the $PCS@Bi_2WO_6$ composites exhibit much enhanced photocatalytic performance under irradiation of simulated sunlight (especially in the UV region). On the other hand, PCS is excited by the visible-light absorption, and the photoexcited electrons could also take part in the photocatalytic reactions. This is the secondary reason resulting in the enhanced photocatalytic performance of the $PCS@Bi_2WO_6$ composites (especially in the visible-light region). The enough positive VB potential of Bi_2WO_6 (+3.12 V vs NHE) means that the photogenerated VB holes in Bi_2WO_6 can react with H_2O or OH^- to generate •OH ($E^0(H_2O/•OH) = +2.38$ V vs NHE, $E^0(OH^-/•OH) = +1.99$ V vs NHE (Gao et al., 2019; He et al., 2016). However, •OH plays only a minor role in the degradation of RhB according to the reactive species trapping experiments, whereas direct hole oxidation is confirmed to be a main mechanism casing the dye degradation. •O_2^- is also determined to an important reactive species in the photocatalysis. The production of •O_2^- could be derived from the combination of adsorbed O_2 with the photoexcited e$^-$ at higher excited states of Bi_2WO_6 or in PCS. It is noted that, however, the photogenerated e$^-$ in the CB of Bi_2WO_6 can not react with O_2 to produce •O_2^- since the CB potential of Bi_2WO_6 (+0.19 V vs NHE) is not negative to the O_2/•O_2^- (−0.13 V vs NHE) (Di et al., 2019).

4. Conclusions

Bi_2WO_6 nanoparticles (average size: ~85 nm) have been successfully assembled on the surface of honeycomb-like PCS (average pore size: ~2 μm) via a hydrothermal route. The achieved $PCS@Bi_2WO_6$ hybrid composite photocatalysts exhibit an excellent photocatalytic degradation of RhB under simulated sunlight irradiation. Especially, the
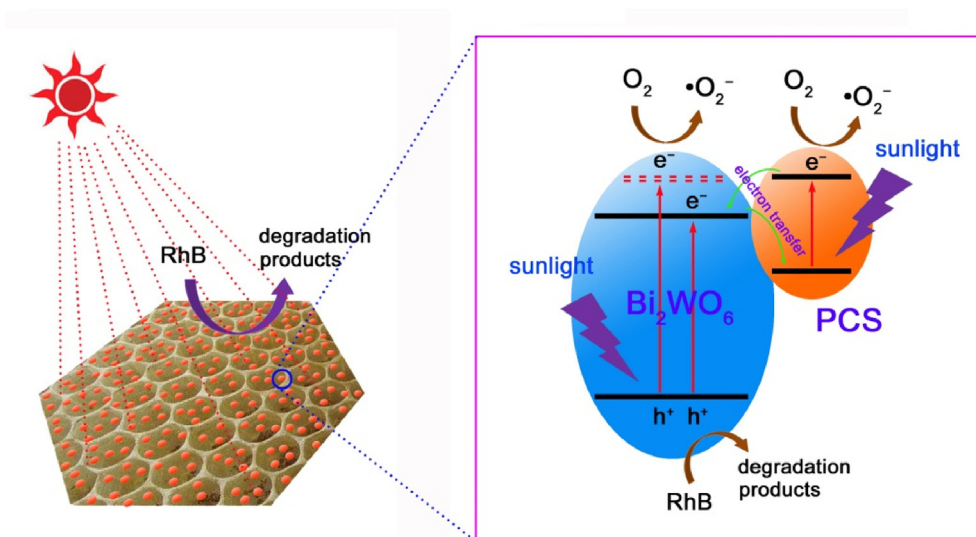
Fig. 11. Schematic illustration of the photocatalytic mechanism of the PCS@Bi$_2$WO$_6$ composites.

5 wt%PCS@Bi$_2$WO$_6$ composite with a PCS mass fraction of 5% manifests a photocatalytic activity about 2.1 times larger than that of bare Bi$_2$WO$_6$ nanoparticles. There are two key factors for the enhanced photocatalytic activity of the PCS@Bi$_2$WO$_6$ hybrid composites. One is that the electron transfer between Bi$_2$WO$_6$ and PCS promotes the separation of photoproduced e$^-$/h$^+$ pairs in Bi$_2$WO$_6$. The other is that the visible-light excited electrons in PCS could also cause the dye gradation, thus increasing the visible-light utilization. Photogenerated holes and •O$_2^-$ radicals are determined, from the active species trapping experiments, to be the dominant reactive species. Moreover, the composite photocatalysts also exhibit a good reusability for the photocatalytic degradation of the dye. However, in the present PCS@Bi$_2$WO$_6$ hybrid composites, the aggregation phenomenon of Bi$_2$WO$_6$ particles still need to be solved, so as to achieve a much better photocatalytic performance.

Acknowledgements

Appendix A. Supplementary data

Supplementary data to this article can be found online at https://doi.org/10.1016/j.jenvman.2019.109341.

References

Akpan, U.G., Hameed, B.H., 2009. Parameters affecting the photocatalytic degradation of dyes using TiO$_2$-based photocatalysts: a review. J. Hazard Mater. 170, 520–529.

Ahmadi, M., Motlagh, H.R., Jaafarzadeh, N., Mostoufi, A., Saeedi, R., Barzegar, G., Jorfi, S., 2017. Enhanced photocatalytic degradation of tetracycline and real pharmaceutical wastewater using MWCNT/TiO2 nano-composite, vol. 186. pp. 55–63.

Bi, T.T., Fang, H.Q., Jiang, J.L., He, XXb, Zhen, X., Yang, H., Wei, Z.Q., Jia, Z.F., 2019. Enhance supercapacitive performance of MnO$_2$/3D carbon nanotubesgraphene as a binder-free electrode. J. Alloy. Comp. 787, 759–766.

Brown, M.A., De Vito, S.C., 1993. Predicting azo dye toxicity. Crit. Rev. Environ. Sci. Technol. 23, 249–324.

Cardon, F., Gomes, W.P., 1978. On the determination of the flat-band potential of a semiconductor in contact with a metal or an electrolyte from the Mott-Schottky plot. J. Phys. D Appl. Phys. 11, L63–L67.

Cen, C.L., Zhang, Y.B., Liang, C.P., Chen, X.F., Yi, Z., Duan, T., Tang, Y.J., Ye, X., Yi, Y.G., Xiao, S.Y., 2019a. Numerical investigation of a tunable dual-band metamaterial perfect absorber consisting of two-intersecting graphene nanorings arrays. Phys. Lett. A. https://doi.org/10.1016/j.physleta.2019.06.028.

Cen, C.L., Yi, Z., Zhang, G.F., Zhang, Y.B., Liang, C.P., Chen, X.F., Tang, Y.J., Ye, X., Yi, Y.G., Wang, J.Q., Hua, J.J., 2019b. Theoretical design of a triple-band perfect metamaterial absorber in the THz frequency range. Result. Phys. 14, 102463.

Chen, J.S., Hua, X., Mao, C.J., Niu, H.L., Song, J.M., 2018. Synthesis of monodisperse pancake-like Bi$_2$WO$_6$ with prominent photocatalytic performances. Res. Chem. Inter. Mediat. 44, 2251–2259.

Cheng, T.Q., Griffiths, K., Norton, P.R., Puddephatt, R.J., 1998. XPS studies of copper deposition from 1,5-cyclooctadiene-copper(I)-hexafluoroacetylacetonate on Si(111). Appl. Surf. Sci. 126, 303–308.

Chong, B., Chen, L., Wang, W.T., Han, D.Z., Wang, L., Feng, L.J., Li, Q., Li, C.H., 2017. Visible-light-driven Ag-decorated g-C$_3$N$_4$/Bi$_2$WO$_6$ Z-scheme composite for high photocatalytic activity. Mater. Lett. 204, 149–153.

Cruz-Ortiz, B.R., Hamilton, J.W.J., Pablos, C., Diaz-Jimenez, L., Cortes-Hernandez, D.A., Sharma, P.K., Castro-Alferez, M., Fernandez-Ibanez, P., Dunlop, P.S.M., Byrne, J.A., 2017. Mechanism of photocatalytic disinfection using titania-graphene composites under UV and visible irradiation. Chem. Eng. J. 316, 179–186.

Di, L.J., Yang, H., Xian, T., Chen, X.J., 2018a. Construction of Z-scheme g-C$_3$N$_4$/CNT/Bi$_2$Fe$_4$O$_9$ composites with improved simulated-sunlight photocatalytic activity for the dye degradation. Micromachines 9, 613.

Di, L.J., Yang, H., Xian, T., Chen, X.J., 2018b. Facile synthesis and enhanced visible-light photocatalytic activity of novel p-Ag$_3$PO$_4$/n-BiFeO$_3$ heterojunction composites for dye degradation. Nanoscale Res. Lett. 13, 257.

Di, L.J., Yang, H., Xian, T., Liu, X.Q., Chen, X.J., 2019. Photocatalytic and photo-Fenton catalytic degradation activities of Z-scheme Ag$_2$S/BiFeO$_3$ heterojunction composites under visible-light irradiation. Nanomaterials 9, 399.

Devi1, P., Thakur, A., Bhardwaj, S.K., Saini, S., Rajput, P., Kumar, P., 2018. Metal ion sensing and light activated antimicrobial activity of aloevera derived carbon dots. J. Mater. Sci. Mater. Electron. 29, 17254–17261.

Etogo, A., Liu, R., Ren, J.B., Qi, L.W., Zheng, C.C., Ning, J.Q., Zhong, Y.J., Hu, Y., 2016. Facile one-pot solvothermal preparation of Mo-doped Bi$_2$WO$_6$ biscuit-like microstructures for visible-light-driven photocatalytic water oxidation. J. Mater. Chem. 4, 13242–13250.

Fattah-alhosseini, A., 2016. Passivity of AISI 321 stainless steel in 0.5 M H$_2$SO$_4$ solution studied by Mott–Schottky analysis in conjunction with the point defect model. Arab J. Chem. 9, S1342–S1348.

Fernando, K.A.S., Sahu, S.P., Liu, Y., Lewis, W.K., Guliants, E., Jafariyan, A., Wang, P., Bunker, C.E., Sun, Y.P., 2015. Carbon quantum dots and applications in photocatalytic energy conversion. ACS Appl. Mater. Interfaces 7, 8363–8376.

Gao, H.J., Wang, F., Wang, S.F., Wang, X.X., Yi, Z., Yang, H., 2019. Photocatalytic activity tuning in a novel Ag$_2$S/CQDs/CuBi$_2$O$_4$ composite: synthesis and photocatalytic mechanism. Mater. Res. Bull. 115, 140–149.

He, Z., Sun, X.Y., Gu, X., 2017. SrTiO$_3$ nanoparticles and nanofibers: synthesis and comparison of photocatalytic properties. J. Mater. Sci. Mater. Electron. 28, 13950–13955.

He, Z.M., Xia, Y.M., Tang, B., Jiang, X.F., Su, J.B., 2016. Fabrication and photocatalytic property of ZnO/Cu$_2$O core-shell nanocomposites. Mater. Lett. 184, 148–151.

Hojamberdiev, M., Kadirova, Z.C., Goncalves, R.V., Yubuta, K., Matsushita, N., Teshima, K., Hasegawa, M., Okada, K., 2018. Reduced graphene oxide-modified Bi$_2$WO$_6$/BiOI composite for the effective photocatalytic removal of organic pollutants and molecular modeling of adsorption. J. Mol. Liq. 268, 715–727.

Issarapanacheewin, S., Wetchakun, K., Phanichphant, S., Kangwansupamonkon, W., Wetchakun, N., 2016. Efficient photocatalytic degradation of Rhodamine B by a novel CeO$_2$/Bi$_2$WO$_6$ composite film. Catal. Today 278, 280–290.

Jiang, J.L., He, X.X., Du, J.F., Pang, X.J., Yang, H., Wei, Z.Q., 2018. In-situ fabrication of

graphene-nickel matrix composites. Mater. Lett. 220, 178–181.

Khataeea, A.R., Kasiri, M.B., 2010. Photocatalytic degradation of organic dyes in the presence of nanostructured titanium dioxide: influence of the chemical structure of dyes. J. Mol. Catal. A Chem. 28, 8–26.

Konstantinou, I.K., Albanis, T.A., 2004. TiO₂-assisted photocatalytic degradation of azo dyes in aqueous solution: kinetic and mechanistic investigations: a review. Appl. Catal. B Environ. 49, 1–14.

Kuo, C.Y., Wu, C.H., Hsu, M.J., 2018. Solvothermal synthesis of carbon nanotubes/ Bi₂WO₆ composites to improve photocatalytic activity of Bi₂WO₆. Desalin. Water Treat. 106, 116–124.

Liu, Y.J., Cai, R., Fang, T., Wu, J.G., Wei, A., 2015. Low temperature synthesis of Bi₂WO₆ and its photocatalytic activities. Mater. Res. Bull. 66, 96–100.

Lv, Y.H., Yao, W.Q., Zong, R.L., Zhu, Y.F., 2016. Fabrication of wide-range-visible pho-tocatalyst Bi₂WO₆₋ₓ nanoplates via surface oxygen vacancies. Sci. Rep. 6, 19347.

Li, J., Ni, G., Han, Y., Ma, Y.M., 2017. Synthesis of La doped Bi₂WO₆ nanosheets with high visible light photocatalytic activity. J. Mater. Sci. Mater. Electron. 28, 10148–10157.

Li, H.T., Kang, Z.H., Liu, Y., Lee, S.T., 2012. Carbon nanodots: synthesis, properties and applications. J. Mater. Chem. 22, 24230–24253.

Mahdiani, M., Soofivand, F., Ansari, F., Salavati-Niasari, M., 2018. Grafting of CuFe₁₂O₁₉ nanoparticles on CNT and graphene: eco-friendly synthesis, characterization and photocatalytic activity. J. Clean. Prod. 176, 185–1197.

Ma, D., Wu, J., Gao, M.C., Xin, Y.J., Ma, T.J., Sun, Y.Y., 2016. Fabrication of Z-scheme g-C₃N₄/RGO/Bi₂WO₆ photocatalyst with enhanced visible-light photocatalytic activity. Chem. Eng. J. 290, 136–146.

Mert, B.D., Mert, M.E., Kardas, G., Yazici, B., 2012. Experimental and theoretical studies on electrochemical synthesis of poly(3-amino-1,2,4-triazole). Appl. Surf. Sci. 258, 9668–9674.

Moulder, J.F., Stickle, W.F., Sobol, P.E., Bomben, K.D., 1992. Handbook of X-Ray Photoelectron Spectroscopy. Perkin-Elmer, Eden Prairie, MN).

Oshikiri, M., Boero, M., Ye, J.H., Zou, Z.G., Kido, G.Y., 2002. Electronic structures of promising photocatalysts InMO₄ (M = V, Nb, Ta) and BiVO₄ for water decomposition in the visible wavelength region. J. Chem. Phys. 117, 7313–7318.

Panmand, R.P., Sethi, Y.A., Kadam, S.R., Tamboli, M.S., Nikam, L.K., Ambekar, J.D., Park, C.J., Kale, B.B., 2015. Self-assembled hierarchical nanostructures of Bi₂WO₆ for hy-drogen production and dye degradation under solar light. CrystEngComm 17, 107–115.

Phuruangrat, A., Maneechote, A., Dumrongrojthanath, P., Ekthammathat, N., Thongtem, S., Thongtem, T., 2015. Visible-light driven photocatalytic degradation of rhodamine B by Ag/Bi₂WO₆ heterostructures. Mater. Lett. 159, 289–292.

Pooladi, M., Shokrollahi, H., Lavasani, S.A.N.H., Yang, H., 2019. Investigation of the structural, magnetic and dielectric properties of Mn-doped Bi₂Fe₄O₉ produced by reverse chemical co-precipitation. Mater. Chem. Phys. 229, 39–48.

Reddy, K.R., Reddy, C.V., Nadagouda, M.N., Shetti, N.P., Jaesool, S., Aminabhavi, T.M., 2019. Polymeric graphitic carbon nitride (g-C₃N₄)-based semiconducting nanos-tructured materials: synthesis methods, properties and photocatalytic applications. J. Environ. Manag. 238, 25–40.

Seddigi, Z.S., Gondal, M.A., Rashid, S.G., Abdulaziz, M.A., Ahmed, S.A., 2016. Facile synthesis and catalytic performance of nanosheet–nanorods g-C₃N₄-Bi₂WO₆ hetero-junction catalyst and effect of silver nanoparticles loading on bare Bi₂WO₆ and g-C₃N₄-Bi₂WO₆ for N-deethylation process. J. Mol. Catal. A Chem. 420, 167–177.

Sharma, S., Mehta, S.K., Ibhadon, A.O., Kansal, S.K., 2019. Fabrication of novel carbon quantum dots modified bismuth oxide (α-Bi₂O₃/C-dots): material properties and catalytic applications. J. Colloid Interface Sci. 533, 227–237.

Shad, N.A., Zahoor, M., Bano, K., Bajwa, S.Z., Amin, N., Ihsan, A., Soomro, R.A., Ali, A., Arshad, M.I., Wu, A.G., 2017. Synthesis of flake-like bismuth tungstate (Bi₂WO₆) for photocatalytic degradation of coomassie brilliant blue (CBB). Inorg. Chem. Commun. 86, 213–217.

Shirzad-Siboni, M., Jonidi-Jafari, A., Farzadkia, M., Esrafili, A., Gholami, M., 2017. Enhancement of photocatalytic activity of Cu-doped ZnO nanorods for the degrada-tion of an insecticide: kinetics and reaction pathways. J. Environ. Manag. 186, 1–11.

Sing, K.S.W., Williams, R.T., 2004. Physisorption hysteresis loops and the characteriza-tion of nanoporous materials. Adsorpt. Sci. Technol. 22, 773–782.

Tayyebi, A., Soltani, T., Hong, H., Lee, B.K., 2018. Improved photocatalytic and photo-electrochemical performance of monoclinic bismuth vanadate by surface defect states (Bi₁₋ₓVO₄). J. Colloid Interface Sci. 514, 565–575.

Tiwari, A., Shukla, A., Lalliansanga, Tiwari, D., Lee, S.M., 2018. Nanocomposite thin films Ag-0(NP)/TiO₂ in the efficient removal of micro-pollutants from aqueous solutions: a case study of tetracycline and sulfamethoxazole removal. J. Environ. Manag. 220, 96–108.

Tong, H., Xu, Y.Q., Su, Y.W., Wang, X.X., 2019. Theoretical study for fabricating elliptical subwavelength nanohole arrays by higher-order waveguide-mode interference. Result. Phys. 14, 102460.

Wang, H., Zhang, Y., Ma, Z., Zhang, W.J., 2019a. Role of PEG2000 on sol-gel preparation of porous La₂Ti₂O₇ for enhanced photocatalytic activity on ofloxacin degradation. Mater. Sci. Semicond. Process. 91, 151–158.

Wang, S.F., Gao, H.J., Wei, Y., Li, Y.W., Yang, X.H., Fang, L.M., Lei, L., 2019b. Insight into the optical, color, photoluminescence properties, and photocatalytic activity of the N-O and C-O functional groups decorating spinel type magnesium aluminate. CrystEngComm 21, 263–277.

Wang, X.X., Zhu, J.K., Tong, H., Yang, X.D., Wu, X.X., Pang, Z.Y., Yang, H., Qi, Y.P., 2019c. A theoretical study of a plasmonic sensor comprising a gold nano-disk array on gold film with an SiO₂ spacer. Chin. Phys. B 28, 044201.

Wang, X.X., Bai, X.L., Pang, Z.Y., Zhu, J.K., Wu, Y., Yang, H., Qi, Y.P., Wen, X.L., 2019d. Surface-enhanced Raman scattering by composite structure of gold nanocube-PMMA-gold film. Opt. Mater. Express 9, 1872–1881.

Wang, X.X., Zhu, J.K., Wen, X.L., Wu, X.X., Wu, Y., Su, Y.W., Tong, H., Qi, Y.P., Yang, H., 2019e. Wide range refractive index sensor based on a coupled structure of Au na-nocubes and Au film. Opt. Mater. Express 9, 3079–3088.

Wang, X., Pang, Z.Y., Yang, H., Qi, Y.P., 2019f. Theoretical study of subwavelength cir-cular grating fabrication based on continuously exposed surface plasmon interference lithography. Result. Phys. 14, 102446.

Wang, S.Y., Yang, H., Wang, X.X., Feng, W.J., 2019g. Surface disorder engineering of flake-like Bi₂WO₆ crystals for enhanced photocatalytic activity. J. Electron. Mater. 48, 2067–2076.

Wang, S.F., Gao, H.J., Fang, L.M., Wei, Y., Li, Y.W., Lei, L., 2019h. Synthesis and char-acterization of BaAl₂O₄ catalyst and its photocatalytic activity towards degradation of methylene blue dye. Z. Phys. Chem. https://doi.org/10.1515/zpch-2018-1308.

Xia, Y., He, Z., Su, J., Liu, Y., Tang, B., 2018a. Fabrication and photocatalytic property of novel SrTiO₃/Bi₅O₇I nanocomposites. Nanoscale Res. Lett. 13, 148.

Xia, Y.M., He, Z.M., Hu, K.J., Tang, B., Su, J.B., Liu, Y., Li, X.P., 2018b. Fabrication of n-SrTiO₃/p-Cu₂O heterojunction composites with enhanced photocatalytic perfor-mance. J. Alloy. Comp. 753, 356–363.

Xie, R.Y., Zhang, L.P., Liu, H.C., Xu, H., Zhong, Y., Sui, X.F., Mao, Z.P., 2017. Construction of CQDs-Bi₂₀TiO₃₂/PAN electrospun fiber membranes and their photocatalytic ac-tivity for isoproturon degradation under visible light. Mater. Res. Bull. 94, 7–14.

Yan, Y.X., Yang, H., Zhao, X.X., Li, R.S., Wang, X.X., 2018a. Enhanced photocatalytic activity of surface disorder-engineered CaTiO₃. Mater. Res. Bull. 105, 286–290.

Yan, Y.X., Yang, H., Zhao, X.X., Zhang, H.M., Jiang, J.L., 2018b. A hydrothermal route to the synthesis of CaTiO₃ nanocuboids using P25 as the titanium source. J. Electron. Mater. 47, 3045–3050.

Yan, Y.X., Yang, H., Yi, Z., Li, R.S., Wang, X.X., 2019. Enhanced photocatalytic perfor-mance and mechanism of Au@CaTiO₃ composites with Au nanoparticles assembled on CaTiO₃ nanocuboids. Micromachines 10, 254.

Yang, Z., Yang, H.J., Yang, H.S., 2018. Effects of sucrose addition on the rheology and microstructure of k-carrageenan gel. Food Hydrocolloids 75, 164–173.

Ye, Y.C., Yang, H., Zhang, H.M., Jiang, J.L., 2019. A promising Ag₂CrO₄/LaFeO₃ het-erojunction photocatalyst applied to photo-Fenton degradation of RhB. Environ. Technol. https://doi.org/10.1080/09593330.2018.1538261.

Yi, Z., Huang, J., Cen, C.L., Chen, X.F., Zhou, Z.G., Tang, Y.J., Wang, B.Y., Yi, Y.G., Wang, J., Wu, P.H., 2019a. Nanoribbon-ring cross perfect metamaterial graphene multi-band absorber in THz range and the sensing application. Result. Phys. 14, 102367.

Yi, Z., Liang, C.P., Chen, X.F., Zhou, Z.G., Tang, Y.J., Ye, X., Yi, Y.G., Wang, J.Q., Wu, P.H., 2019b. Dual-band plasmonic perfect absorber based on graphene metamaterials for refractive index sensing application. Micromachines 10, 443.

Yu, B.Y., Kwak, S.Y., 2012. Carbon quantum dots embedded with mesoporous hematite nanospheres as efficient visible light-active photocatalysts. J. Mater. Chem. 22, 8345–8353.

Yu, H.G., Chu, C.L., An, X.L., 2019. Enhanced visible-light-driven photocatalytic activity of F doped reduced graphene oxide-Bi₂WO₆ photocatalyst. Appl. Organomet. Chem. 33, e4682.

Zhang, Z.J., Zheng, T.T., Xu, J.Y., Zeng, H.B., Zhang, N., 2017. Carbon quantum dots/ Bi₂WO₆ composites for efficient photocatalytic pollutant degradation and hydrogen evolution. Nano 12, 1750082.

Zhang, Y.B., Cen, C.L., Liang, C.P., Yi, Z., Chen, X.F., Li, M.W., Zhou, Z.G., Tang, Y.J., Yi, Y.G., Zhang, G.F., 2019. Dual-band switchable terahertz metamaterial absorber based on metal nanostructure. Result. Phys. 14, 102422.

Zhao, W.H., Wei, Z.Q., Zhang, L., Wu, X.J., Wang, X., 2018a. Cr doped SnS₂ nanoflowers: preparation, characterization and photocatalytic decolorization. Mater. Sci. Semicond. Process. 88, 173–180.

Zhao, X.X., Yang, H., Li, S.H., Cui, Z.M., Zhang, C.R., 2018b. Synthesis and theoretical study of large-sized Bi₄Ti₃O₁₂ square nanosheets with high photocatalytic activity. Mater. Res. Bull. 107, 180–188.

Zhao, X.X., Yang, H., Zhang, H.M., Cui, Z.M., Feng, W.J., 2019a. Surface-disorder-en-gineering-induced enhancement in the photocatalytic activity of Bi₄Ti₃O₁₂ na-nosheets. Desalin. Water Treat. 145, 326–336.

Zhao, X., Yang, H., Cui, Z., Yi, Z., Yu, H., 2019b. Synergistically enhanced photocatalytic performance of Bi₄Ti₃O₁₂ nanosheets by Au and Ag nanoparticles. J. Mater. Sci. Mater. Electron. 30, 13785–13796. https://doi.org/10.1007/s10854-019-01762-7.

Zhao, X.X., Yang, H., Li, R.S., Cui, Z.M., Liu, X.Q., 2019c. Synthesis of heterojunction photocatalysts composed of Ag₂S quantum dots combined with Bi₄Ti₃O₁₂ nanosheets for the degradation of dyes. Environ. Sci. Pollut. Res. 26, 5524–5538.

Zheng, C.X., Yang, H., Cui, Z.M., Zhang, H.M., Wang, X.X., 2017. A novel Bi₄Ti₃O₁₂/ Ag₃PO₄ heterojunction photocatalyst with enhanced photocatalytic performance. Nanoscale Res. Lett. 12, 608.

Zheng, C.X., Yang, H., 2018. Assembly of Ag₃PO₄ nanoparticles on rose flower-like Bi₂WO₆ hierarchical architectures for achieving high photocatalytic performance. J. Mater. Sci. Mater. Electron. 29, 9291–9300.

Zhou, Y.X., Meng, X.D., Tong, L., Zeng, X.H., Chen, X.B., 2016. Template-free fabrication of Bi₂WO₆ hierarchical hollow microspheres with visible-light-driven photocatalytic activity. Energies 9, 764.

Zhu, X.L., Wei, Z.Q., Zhao, W.H., Zhang, X.D., Zhang, L., Wang, X., 2018. Microstructure and electrochemical properties of ZnMn₂O₄ nanopowder synthesized using different surfactants. J. Electron. Mater. 47, 6428–6436.